



**HAL**  
open science

# Matched absorbing medium techniques for full-wave TLM simulations of microwave and millimeter-wave components

Sandrick Le Maguer, Nestor Pena, Michel Ney

## ► To cite this version:

Sandrick Le Maguer, Nestor Pena, Michel Ney. Matched absorbing medium techniques for full-wave TLM simulations of microwave and millimeter-wave components. *Annals of Telecommunications - annales des télécommunications*, 1998, 53 (3/4), pp.115-129. 10.1007/BF02998569 . hal-02399374

**HAL Id: hal-02399374**

**<https://hal.science/hal-02399374>**

Submitted on 8 Apr 2022

**HAL** is a multi-disciplinary open access archive for the deposit and dissemination of scientific research documents, whether they are published or not. The documents may come from teaching and research institutions in France or abroad, or from public or private research centers.

L'archive ouverte pluridisciplinaire **HAL**, est destinée au dépôt et à la diffusion de documents scientifiques de niveau recherche, publiés ou non, émanant des établissements d'enseignement et de recherche français ou étrangers, des laboratoires publics ou privés.



Distributed under a Creative Commons Attribution - NonCommercial 4.0 International License

# Matched absorbing medium techniques for full-wave TLM simulation of microwave and millimeter-wave components

Sandrick LE MAGUER\*,  
Nestor PEÑA\*,  
Michel NEY\*

## Abstract:

*This paper investigates the absorbing layer techniques for three-dimensional transmission-line matrix (3D-TLM) simulations. Applications are the full-wave analysis of structures such as microwave and millimeter-wave circuits open to free space. Two approaches are presented, namely the matched layer (ML) and the perfectly matched layer (PML) technique which is used for general cases. For the ML technique, which is efficient for matching guides operating in a quasi-TEM condition, a comparison of the different TLM condensed node is carried out. Concerning the more general case of the PML technique, the theoretical development of a new general three-dimensional (3D) TLM condensed cell is presented. Results pertaining to the characterization of planar circuits are compared with other solutions or measurements. It is found that a proposed unified approach, which includes the TLM simulation for matched layer media, yields very good performance in terms of the absorbing boundary condition (ABC).*

Key words : Microwave circuit ; Electromagnetism ; Absorbing medium ; Modeling ; Numerical method ; Transmission line ; Matrix method ; Microstrip line ; Coplanar line ; Impedance matching

*opérant en modes quasi statiques, est étudiée dans le cas de différents types de cellules TLM condensées. Pour la simulation des milieux PML applicables aux cas plus généraux, le développement théorique d'une nouvelle cellule TLM tridimensionnelle est présenté. Dans le cadre de caractérisation de discontinuités en technologie plaquée, des résultats de simulations sont comparés avec des solutions trouvées par d'autres méthodes ou la mesure. On trouve que l'approche unifiée proposée donne de très bonnes performances en termes de conditions absorbantes aux limites (ABC).*

Mots clés : Circuit hyperfréquence ; Electromagnétisme ; Milieu absorbant ; Modélisation ; Méthode numérique ; Ligne transmission ; Méthode matricielle ; Ligne microruban ; Ligne coplanaire ; Adaptation impédance

## Contents

- I. Introduction
  - II. The TLM method
  - III. Absorbing layer theory
  - IV. Implementation in the TLM algorithm
  - V. Results
  - VI. Conclusions
- Appendix  
References (23 ref.)

---

## TECHNIQUE DES COUCHES ABSORBANTES ADAPTÉES, APPLIQUÉES À L'ANALYSE RIGOUREUSE DES COMPOSANTS MICROONDES ET EN BANDE MILLIMÉTRIQUE, PAR LA MÉTHODE TLM

---

## Résumé :

*Cet article présente des techniques des milieux absorbants pour la modélisation par la méthode de la matrice des lignes de transmission tridimensionnelle (3D-TLM). Les applications sont l'analyse électromagnétique de circuits microondes et millimétriques ouverts sur l'espace libre. Les deux approches discutées utilisent les milieux adaptés (ML) et les couches parfaitement adaptées (PML), ces dernières étant utilisées pour le cas général. La technique ML, qui est efficace pour l'adaptation de guides*

## I. INTRODUCTION

The TLM method has been widely used for field computations in the time domain. It is a general method that can be applied to a wide class of problems, including non linear and/or non-stationary cases [1]-[2]. However, like any method whose formulation leads to volume discretization, absorbing boundary conditions (ABC) must be used to limit the computational domain when open structures are investigated. These structures can be, for instance, open to free space (antenna) or of infinite extend (e.g., waveguide discontinuity problems). Generally, ABC should have absorb waves over a wide fre-

---

\* Laboratoire d'électronique et de systèmes de télécommunications (LEST) UMR CNRS no. 6616  
École Nationale Supérieure des Télécommunications de Bretagne (ENST-Br.) BP 832 - F29285 Brest Cedex, France

quency range and at any incident angle. They are usually classified into two groups: those based on boundary operators and those using absorbing layer techniques. For TLM, the most popular boundary operators are based on one-way equation solutions [3, 4] or extrapolation techniques [5]. Their algorithm is applied to the limiting boundary where field values at future time are computed by linear combination of field values in the computational domain at different locations and previous time steps. Algorithms are rather simple to apply but these techniques yield numerical instabilities under certain conditions and regularization procedures must be applied to obtain stable results [3]. In addition, such ABC should be located at relatively large distances from scatterers as they cannot absorb evanescent waves.

Concerning absorbing layer techniques, equations governing fields in the lossy layer, terminated by certain arbitrary boundary conditions, must be solved by a numerical scheme. Therefore, the computational domain must be extended, unlike the boundary operator approach. For instance, the so-called matched layer (ML) technique consists in surrounding the computational domain with a layer of fictitious lossy medium with electric and magnetic conductivities which are chosen accordingly. This technique yields excellent results for any frequency when normal incidence is approximately achieved [6]. This condition arises, for instance, for matched load simulations of guides operating under quasi-TEM conditions. In addition, the ML technique has the great advantage of being inherently stable and the layer medium can be directly modeled by the standard symmetrical condensed node (SCN) without extra programming.

The extension of the ML technique to operate for arbitrary incidence yields to the perfectly matched layer (PML) technique, which was first proposed by Bérenger for finite-difference time-domain (FDTD) computations [7]-[8]. The layer surrounding the computational domain is perfectly matched in the sense that electromagnetic waves, whether traveling or evanescent, theoretically penetrate into it with no reflection and refraction in all cases of incidence and at arbitrary frequency. The implementation of the PML technique in the FDTD scheme is straightforward as the layer equations are directly written in a difference form using the standard Yee's algorithm [7]. Concerning the PML-TLM case, two different approaches can be considered:

- interfacing the TLM-computational network with FDTD mesh simulating the PML medium (non-unified or split algorithm) [9]-[10].
- using a TLM node in the PML medium (unified algorithm) [11].

The second approach has the potential advantage of avoiding field spatial interpolation which is required to interface TLM and FDTD algorithms. Indeed, it is well known that field components are not defined at the same location in both cells. One objective of this paper is to present a new TLM node that can simulate PML media with the objective to use a unified algorithm for PML used as ABC. To develop this new node, the PML field

equations are rewritten such as to establish Maxwell's equations pertaining to an anisotropic lossy medium with sources and characterized by real diagonal electric and magnetic conductivity tensors. Magnetic and electric current source densities are controlled by field spatial time variations [11]-[13]. Then, using a rigorous field formulation [14], equations are approximated while keeping TLM formalism, i.e., in terms of incident and reflected voltages that travel in the network of interconnected nodes which simulates the PML medium.

## II. THE TLM METHOD

The TLM method is a time-domain numerical technique that models an electromagnetic field in a computational domain by means of voltage impulses that travel in a network of interconnected transmissions lines. More fundamentally, the TLM network is able to model Maxwell-Ampère (MA) and Maxwell-Faraday (MF) laws in presence of electric  $\vec{J}_e$  and magnetic  $\vec{J}_m$  current densities in lossy media [14]. These two equations in local form are given respectively by:

$$(1) \quad \nabla \wedge \vec{H} = \hat{\epsilon} \frac{\partial \vec{E}}{\partial t} + \hat{\sigma}_e \vec{E} + \vec{J}_e$$

$$(2) \quad \nabla \wedge \vec{E} = -\hat{\mu} \frac{\partial \vec{H}}{\partial t} - \hat{\sigma}_m \vec{H} - \vec{J}_m$$

in which  $\hat{\epsilon}$ ,  $\hat{\mu}$ ,  $\hat{\sigma}_e$  and  $\hat{\sigma}_m$  are real diagonal tensors of permittivity, permeability, electric and magnetic conductivities, respectively, given by:

$$(3) \quad \hat{\epsilon} = \epsilon_0 \text{diag}(\epsilon_{xx}, \epsilon_{yy}, \epsilon_{zz}), \hat{\mu} = \mu_0 \text{diag}(\mu_{xx}, \mu_{yy}, \mu_{zz}),$$

$$(4) \quad \hat{\sigma}_e = \text{diag}(\sigma_{ex}, \sigma_{ey}, \sigma_{ez}), \hat{\sigma}_m = \text{diag}(\sigma_{mx}, \sigma_{my}, \sigma_{mz}),$$

and  $\epsilon_0$ ,  $\mu_0$  are vacuum permittivity and permeability, respectively.

The computational domain is then filled with a Cartesian mesh of cells with dimension  $\Delta_x$ ,  $\Delta_y$ ,  $\Delta_z$ . In each cell,  $\vec{E}$  and  $\vec{H}$  tangential components are sampled at the center of every face as well as total field components at the center, as illustrated by Figure 1a and 1b, respectively. There is a total of 15 samples for each field which can be combined to generate eighteen incident and reflected voltages which are contained in vectors  $\vec{a}$  and  $\vec{b}$ , respectively. In accordance with the numbering used for the symmetrical condensed TLM-node (SCN) [1], electric field components and voltages are numbered correspondingly, as illustrated by Figure 2a. For instance, samples  $E_1^x$  and  $H_1^z$  are combined in the following way [14]:

$$(5) \quad \begin{Bmatrix} a_1 \\ b_1 \end{Bmatrix} = \frac{1}{2} (\Delta_x E_1^x \pm Z_0 \Delta_z H_1^z)$$

where  $Z_0$  the vacuum intrinsic impedance is  $\sqrt{\mu_0/\epsilon_0}$ . When inhomogenous structures are investigated and/or non-cubic cells are used, so-called permittivity and per-

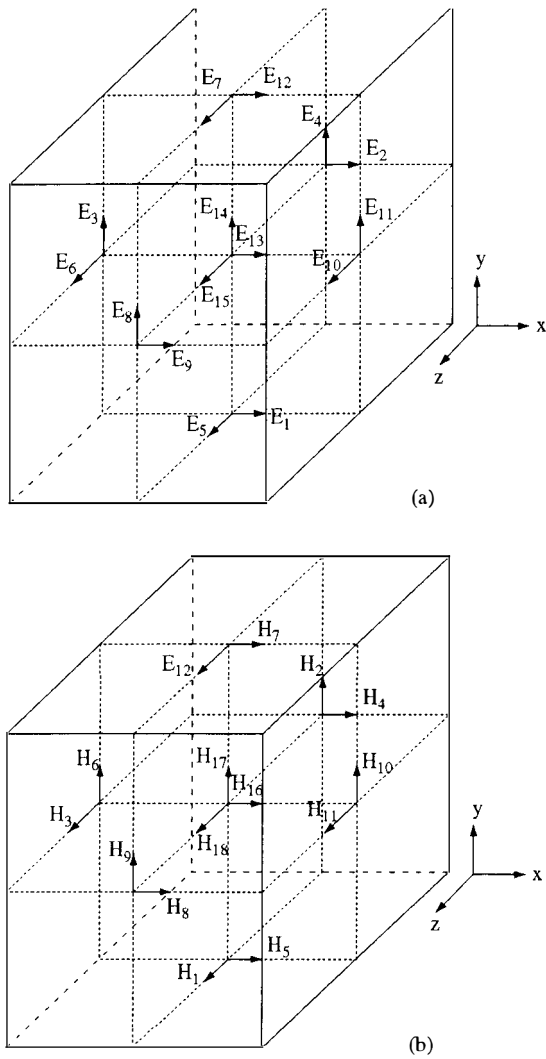


FIG. 1. — Field samples for the basic TLM (SCN) cell : (a) electric field. (b) magnetic field.

Échantillonnage des champs dans la cellule de base TLM (SCN) :  
(a) champ électrique, (b) champ magnétique.

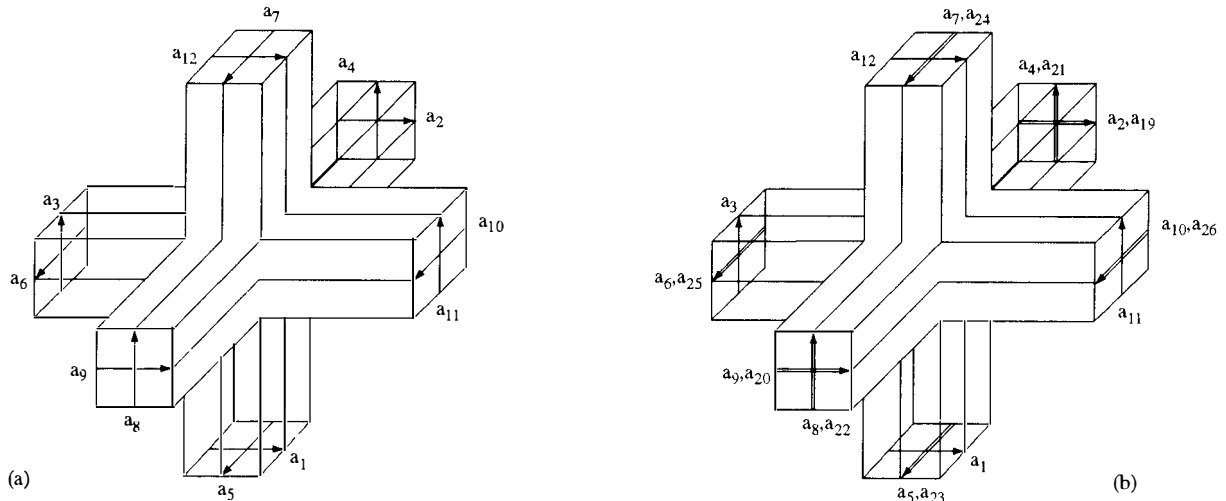


FIG. 2. — Incident voltages in the TLM cell ; (a) basic SCN, (b) new PML-TLM cell.

Tensions incidentes dans la cellule TLM : (a) cellule de base SCN. (b) nouvelle cellule PML-TLM.

meability stubs have to be connected at the center of related nodes. In this case,  $E_x$ ,  $E_y$ ,  $E_z$  take subscript 13, 14, 15, respectively and subscript 16, 17, 18 are assigned to field component  $H_x$ ,  $H_y$ ,  $H_z$  respectively. Hence, a completely loaded SCN includes 18 incident and reflected voltages and can be characterized by a  $18 \times 18$  scattering matrix  $[S]$ . If losses (whether electric and/or magnetic) are present, they can be accounted for by loading the node by three or six infinite (or matched) loss-stubs. As no voltages are reflected from loss-stubs, only  $[S]$ -elements are affected and, thus, the matrix size remains unchanged. Stub voltages are defined from only one field component at the center of the cell. For instance,  $a_{13}$ ,  $b_{13}$ ,  $a_{16}$  and  $b_{16}$  are expressed by :

$$(6) \quad \begin{Bmatrix} a_{13}, b_{13} \\ a_{16}, b_{16} \end{Bmatrix} = \frac{1}{2} \begin{Bmatrix} \Delta_x E_{13}^x \\ Z_0 \Delta_x H_{16}^x \end{Bmatrix}$$

All expressions concerning incident and reflected voltages are included in Appendix A.

Now comes the time-evolution of the TLM algorithm that computes the fields in the structure. First of all, supposing that at time  $(n - 1/2)\Delta t$  the incident voltage vector  $\vec{a}$  is known at every node, then, the reflected voltage  $\vec{b}$  from every node can be computed via  $S$  at time  $(n + 1/2)\Delta t$  as :

$$(7) \quad \vec{b}^{\rightarrow(n+1/2)} = S \vec{a}^{\rightarrow(n-1/2)}$$

in which  $S$  element expression can be found in [1] for the lossless case. Finally, reflected voltages become incident voltages to the neighbouring nodes for the next iteration.

Although the procedure described by (7) is very simple, it is relatively costly in terms of computer expenditure and an accelerated procedure is used instead. First, field components  $\{\vec{E}^n, \vec{H}^n\}$  at the center of the cell are computed at time  $n\Delta t$ . They depend on the

source terms  $\vec{J}_e$  and  $\vec{J}_m$  via expressions that are included in Appendix B. Then, reflected voltages  $\vec{b}$  at time  $(n + 1/2)\Delta t$  are determined from the previously computed  $\{\vec{E}^n, \vec{H}^n\}$  and the incident voltage  $\vec{a}$  which is known at time  $(n - 1/2)\Delta t$  via expressions written in Appendix B. Hence, the matrix  $S$  is not used, which reduces the number of operations per iteration [15].

In TLM, six degrees of freedom are available to consider alternate cells: six stubs or six link-line impedances or any combination thereof. With the objective to reduce the number of stubs and increase the maximum time-step value, Scaramuzza and Lowery [16] proposed the hybrid SCN (HSCN) TLM node that uses only three stubs but needs three different link-line characteristic impedances. Several years later, a new super SCN (SSCN) TLM node that has no stubs was proposed by Trenkic *et al.* [17]. Constitutive parameters and/or parallelepiped cell dimensions are included in six different values of the link-line characteristic impedance. The drawback of these new cells is the interface conditions that must be applied between two different media. However, the reduction in terms of computer costs makes them potentially attractive.

Finally, boundaries are accounted for by using a proper reflection coefficient in the adjacent TLM arm. The value of the reflection coefficients should translate the condition on tangential field components on the boundary. For instance, it is  $-1$  and  $+1$  for perfectly conducting and a magnetic wall, respectively. For other types of physical boundary conditions such as those that yield frequency dependent reflection coefficients, the procedure becomes more complex, yet possible to implement in the TLM scheme (eg., [18]).

### III. ABSORBING LAYER THEORY

#### III.1. Matched layer (ML)

The ML technique consists in enclosing the computational domain (for instance with parameters  $\epsilon_r$  and  $\mu_r$ ) by a lossy passive medium whose constitutive parameters should fulfill the following relation [19]:

$$(8) \quad \frac{\sigma_e}{\epsilon_r \epsilon_0} = \frac{\sigma_m}{\mu_r \mu_0} = S$$

where  $\sigma_e$  and  $\sigma_m$  are the electric and magnetic conductivities of the ML medium, respectively. This lossy medium can be shown to have an intrinsic impedance that corresponds to:

$$(9) \quad Z_m = Z_0 \sqrt{\frac{\mu_r}{\epsilon_r}}$$

As a result, it is perfectly matched for waves that impinge at normal incidence for any frequency. The apparent reflection coefficient (ARC) is evaluated by

considering the wave returning from the back of the layer terminated by an electric wall and expressed in dB by:

$$(10) \quad \text{ARC} = 20 \log(\rho = e^{-\frac{S}{c} 2\delta})$$

where  $\delta$  is the layer thickness and  $c$  the velocity of light in a medium with intrinsic impedance  $Z_m$ .

It has been found that purely numerical reflections exist for a wave propagating through two media with different conductivities but same intrinsic impedance. The level of reflection is proportional to the conductivity difference at the interface. To circumvent this problem, a tapered loss profile is used in the layer, at a price of increasing its thickness  $\delta$ . This approach allows a small difference in conductivities across the interface between the computational domain and the layer, while keeping the same ARC which is now expressed in dB as:

$$(11) \quad 20 \log(\rho = \exp -\frac{2}{c} \int_{z_1}^{z_1+\delta} S(z) dz)$$

for a wave propagating in the (Oz) direction and where  $z_1$  is the coordinate of the interface in the  $xy$ -plane. For the numerical implementation, the conductivity spatial distribution is stepwise approximated such that each cell has constant conductivity value. Thus, the layer can be directly simulated by standard loaded SCN or other more recent nodes such as the HSCN or the SSCN.

#### III.2. Perfectly matched layer (PML)

The PML technique is an extension of the ML and theoretically allows a perfect match for any case of incidence. To achieve good absorption in any direction, Bérenger [7] proposed to split all field components into two sub-terms. For instance, the electric field  $x$ -component is written as  $E_x = E_{xy} + E_{xz}$ . Substituting into (1) and (2) for sourceless situation, leads to a set of twelve equations that can be written in a generic form as [8]:

$$(12) \quad \begin{cases} \epsilon_r \epsilon_0 \frac{\partial E_{\xi\eta}}{\partial t} + \sigma_\eta E_{\xi\eta} = \frac{\partial (H_{\zeta\xi} + H_{\zeta\eta})}{\partial \eta} \\ \epsilon_r \epsilon_0 \frac{\partial E_{\xi\zeta}}{\partial t} + \sigma_\zeta E_{\xi\zeta} = -\frac{\partial (H_{\eta\xi} + H_{\eta\zeta})}{\partial \zeta} \end{cases}$$

$$(13) \quad \begin{cases} \mu_r \mu_0 \frac{\partial H_{\xi\eta}}{\partial t} + \sigma_\eta^* H_{\xi\eta} = -\frac{\partial (E_{\zeta\xi} + E_{\zeta\eta})}{\partial \eta} \\ \mu_r \mu_0 \frac{\partial H_{\xi\zeta}}{\partial t} + \sigma_\zeta^* H_{\xi\zeta} = \frac{\partial (E_{\eta\xi} + E_{\eta\zeta})}{\partial \zeta} \end{cases}$$

where  $(\xi, \eta, \zeta) \in \{(x, y, z), (y, z, x), (z, x, y)\}$  and  $(\sigma_{\eta, \zeta}, \sigma_{\eta, \zeta}^*)$  which are fictitious electric and magnetic conductivities, respectively. These parameters should satisfy (8). Originally, the time evolution of every sub-term is computed in the PML medium using the classical FDTD Yee's scheme. Thus, since these sub-terms are defined at the same location as the corresponding total

component, it is straightforward to transfer the algorithm through the interface between the PML medium and the FDTD computational domain. Hence, a fully unified algorithm can be achieved when FDTD is used.

One can show that a grouped form of (12) and (13) allows the interpretation of a PML medium as a classical lossy medium with controlled current source densities [11]-[13]. For instance, with  $E_x = E_{xy} + E_{xz}$ , (12) can be written in terms of  $(E_x, E_{xy})$  and  $(E_x, E_{xz})$ :

$$(14.a) \quad \varepsilon_r \varepsilon_0 \frac{\partial E_x}{\partial t} + \sigma_z E_x + \{(\sigma_y - \sigma_z)E_{xy}\} = \frac{\partial H_z}{\partial y} - \frac{\partial H_y}{\partial z}$$

$$(14.b) \quad \varepsilon_r \varepsilon_0 \frac{\partial E_{xy}}{\partial t} + \sigma_y E_{xy} = \frac{\partial H_z}{\partial y}$$

$$(15.a) \quad \varepsilon_r \varepsilon_0 \frac{\partial E_x}{\partial t} + \sigma_y E_x + \{(\sigma_z - \sigma_y)E_{xz}\} = \frac{\partial H_z}{\partial y} - \frac{\partial H_y}{\partial z}$$

$$(15.b) \quad \varepsilon_r \varepsilon_0 \frac{\partial E_{xz}}{\partial t} + \sigma_z E_{xz} = - \frac{\partial H_y}{\partial z}$$

Hence, one retrieves (1) for  $E_x$ , with  $\sigma_{ex}$  equal to  $\sigma_z$  and  $\sigma_y$  in (12) and (13), respectively. In addition, the electric current source density  $J_{ex}$  can be identified as  $(\sigma_y - \sigma_z)E_{xy}$  and  $(\sigma_z - \sigma_y)E_{xz}$  in (12) and (13), respectively. Also, one may notice that  $J_{ex}$  is controlled by the  $y$ -spatial variation of  $H_z$  in (12), and by the  $z$ -spatial variation of  $H_y$  in (13).

According to the above observations, one can consider the extension of the SCN to PML medium simulation, if the controlled source evolution can be accounted for by adding appropriate voltages to the basic SCN. This concept was successfully applied to the two-dimensional TLM node [11].

## IV. IMPLEMENTATION IN THE TLM ALGORITHM

### IV.1. ML implementation

Generally,  $S$ -parameter computation requires two simulations. One has the purpose of generating the field solution without the discontinuity (reference or *thru* line). The other simulation performed with the discontinuity inserted, generates the total field solution. This allows the separation of incident and reflected voltages on the guiding structure that feeds the discontinuity under investigation, from which  $S$ -parameter can be computed. A major advantage of time-domain simulations is that  $S$ -parameters are calculated on a wide frequency band by exciting the structure with a narrow impulse (generally gaussian signal). Then, a Fourier transform of the time-domain response is performed to obtain the frequency characterization of the structure.

For the above applications, several precautions must be taken. First of all, input and output ports need to be

matched (infinite line) over the frequency range of interest. Thus, ABC must be placed behind the excitation plane and where a matched load would be connected. Then, points at which the time responses are recorded and should be located far enough from the discontinuity and the excitation plane in such a way that only the dominant mode prevails.

Quasi-TEM mode in microstrip or coplanar waveguide propagates nearly along the longitudinal direction. Thus, these modes impinge almost normally on the plane where ABC is enforced. These features fulfill the basic assumption of using the ML technique. For planar structures, metal strips and substrates are simply extended through the absorbing layer. Then, the mesh is simply terminated in the layer by the intrinsic impedance of the adjacent medium whether it is air or dielectric material (an example is shown in Figure 3). It has been found that better matching is achieved by terminating the layer this way than by a conducting wall as it is usually done in FDTD simulations. Indeed, by terminating the computational domain directly using such conditions, return loss better than 30 dB is achieved. In fact, residual reflections are mainly produced at the interface due to the slight deviation of quasi-TEM modes from normal incidence condition. At the other limits of the computational domain (except if a ground plane is present) the trivial condition, which consists in terminating the TLM mesh by the intrinsic impedance of the adjacent medium, is enforced. If these conditions are applied at locations sufficiently remote from the planar structure where the energy is confined, results are not significantly perturbed. For instance, locating the limit about six to eight cells above the substrate has been found to yield satisfactory results for all practical situations. It is important to mention that using ML instead would not be practical since evanescent waves (reactive fields) predominantly prevail above and on the side of the structure.

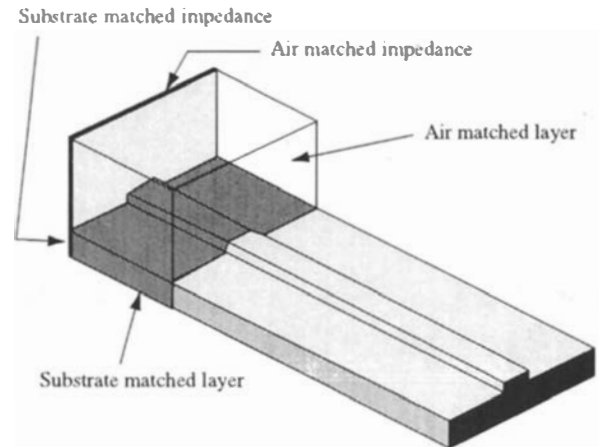


FIG. 3. — Matched layer configuration for microstrip geometry.  
Configuration de la couche adaptée (ML) pour une géométrie de type microruban.

The last condition to be aware of, pertains to the case of non-homogenous matched layers. A condition obtained from Snell-Descartes's law must be taken into account to balance absorption in air and dielectric [20]:

$$(16) \quad \frac{\sigma_1}{\sigma_2} = \frac{\epsilon_1}{\epsilon_2}$$

where  $\sigma_1$ ,  $\epsilon_1$  and  $\sigma_2$ ,  $\epsilon_2$  are adjacent media electric losses and permittivity, respectively. Note that magnetic losses remain the same in all media when dielectric materials only are involved. Finally, losses in the absorbing layer are directly included in the TLM node scattering matrix. In the case of cubic cells, this is done by adding loss (infinitely long) stubs whose characteristic conductance and resistance is given by  $g_e = Z_0 \sigma_e \Delta l$  and  $r_m = \sigma_m \Delta l / Z_0$ , respectively [14].

## IV.2. The PML-TLM cell

Let us consider the interface between the computational domain ( $\epsilon_r, \mu_r$ ) and the PML medium ( $\epsilon_r, \mu_r, \sigma_x, \sigma_x^*, \sigma_y, \sigma_y^*, \sigma_z, \sigma_z^*$ ) perpendicular to the  $z$ -axis. In this case, there is theoretically no reflection at the interface if  $\sigma_x = \sigma_y = \sigma_x^* = \sigma_y^* = 0$  and  $\sigma_z, \sigma_z^*$  satisfy. By setting  $\sigma_y = 0$  into (12) and (13), one can notice an electric loss and current source terms in (14.a). The time evolution of the latter, given by (14.b), is controlled by the magnetic field component normal to the interface. On the other hand, there is only a source term in (15.a) controlled by the spatial variation of magnetic field components tangential to the interface (see (15.b)). By applying the same procedure to other field components, one can derive from (1) and (2) the following relations :

$$(17.a) \quad \nabla \wedge \vec{H} = \epsilon_r \epsilon_0 \frac{\partial \vec{E}}{\partial t} + \hat{\sigma}_{en} \vec{E} + \vec{J}_{en}^{\rightarrow}$$

$$(17.b) \quad \nabla \wedge \vec{H} = \epsilon_r \epsilon_0 \frac{\partial \vec{E}}{\partial t} + \vec{J}_{et}^{\rightarrow}$$

$$(18.a) \quad \nabla \wedge \vec{E} = -\mu_r \mu_0 \frac{\partial \vec{H}}{\partial t} - \hat{\sigma}_{mn} \vec{H} - \vec{J}_{mn}^{\rightarrow}$$

$$(18.b) \quad \nabla \wedge \vec{E} = -\mu_r \mu_0 \frac{\partial \vec{H}}{\partial t} - \vec{J}_{mt}^{\rightarrow}$$

in which subscript e, m pertain to electric and magnetic, respectively and n, t to normal and tangential components to the interface, respectively. Also,  $\hat{\sigma}_{en} = \text{diag}(\sigma_z, \sigma_z^*, 0)$ ,  $\hat{\sigma}_{mn} = \text{diag}(\sigma_x^*, \sigma_x^*, 0)$  and source vectors are given by:

$$(19) \quad \vec{J}_{en}^{\rightarrow} = [-\sigma_z E_{xy} - \sigma_z^* E_{xy}]^T,$$

$$\vec{J}_{mn}^{\rightarrow} = [-\sigma_x^* H_{xy} - \sigma_x^* H_{yx}]^T$$

$$(20) \quad \vec{J}_{et}^{\rightarrow} = [\sigma_z E_{xz} \quad \sigma_z E_{yz}]^T, \quad \vec{J}_{mt}^{\rightarrow} = [\sigma_z^* H_{xz} \quad \sigma_z^* H_{yz}]^T$$

where  $\tau$  denotes transposed vector. Examining (17) to (20) shows that there are different ways to group PML equations. Each yields a different numerical scheme that has specific dispersion characteristics. It has been found that the algorithm implemented in TLM and expressed by (19) and (18.a) yields the best performance in terms of numerical stability and, consequently, is used in the present paper.

### IV.2.1. Numerical scheme

One can notice that  $\hat{\sigma}_e = 0$  and  $\hat{\sigma}_{mn} = \text{diag}(\sigma_x^*, \sigma_x^*, 0)$  present in (17.b) and (18.a) can easily be added in the classical algorithm (see Appendix A), by setting  $A_x = A_y = A_z = 1$ ,  $B_z = 1$  and  $B_x = B_y = B$  in (B.1) to (B.6), where:

$$(21) \quad B = \frac{4}{4 + \hat{R}}, \quad \text{where}, \quad \hat{R} = \frac{1}{Z_0} \frac{\sigma_z^* s}{\mu_r} = Z_0 \frac{\sigma_z^* s}{\epsilon_r},$$

and in which conductivities are deduced from (8). According to relations (B.1) to (B.6) in Appendix B, the source terms must be determined at the cell center and time  $n\Delta t$ . However, they are easily computed as they are proportional to the sub-terms  $E_{xz}$ ,  $E_{yz}$ ,  $H_{xy}$ ,  $H_{yx}$  which are governed by the following equations :

$$(22) \quad \frac{\partial E_{xz}}{\partial t} + Z_0 \frac{c_0 \sigma_z}{\epsilon_r} E_{xz} = -\frac{c_0}{\epsilon_r} Z_0 \frac{\partial H_y}{\partial z}$$

$$(23) \quad \frac{\partial E_{yz}}{\partial t} + Z_0 \frac{c_0 \sigma_z}{\epsilon_r} E_{yz} = \frac{c_0}{\epsilon_r} Z_0 \frac{\partial H_x}{\partial z}$$

$$(24) \quad Z_0 \frac{\partial H_{xy}}{\partial t} = -\frac{c_0}{\mu_r} \frac{\partial E_z}{\partial y}$$

$$(25) \quad Z_0 \frac{\partial H_{yx}}{\partial t} = \frac{c_0}{\mu_r} \frac{\partial E_z}{\partial x}$$

In order to model these sub-terms, one adds two samples per sub-term to the cell illustrated by Figure 1. For instance, the sub-term  $E_{xz}$  involved in (22) needs two samples on faces perpendicular to  $z$ -direction, i.e., at the same locations as  $E_x$  samples with subscript 2 and 9 (see Fig. 1). This is the reason why one uses the notation  $(E_2^{xz}, E_9^{xz})$ . Likewise,  $E_{yz}$  samples involves in (23) are written  $(E_4^{yz}, E_8^{yz})$ ,  $H_{xy}$  samples involves in (24) are written  $(H_3^{xy}, H_7^{xy})$ , and, finally,  $H_{yx}$  samples involved in (25) are written  $(H_6^{yx}, H_{10}^{yx})$ .

Proceeding further with the sub-term  $E_{xz}$ , (22) is numerically integrated between time  $(n - 1/2)\Delta t$  and  $n\Delta t$  as well as between the spatial limits  $(k - 1/2)\Delta z$  and  $(k + 1/2)\Delta z$ , yielding:

$$(26) \quad \Delta_x E_{xz}^n - \frac{T}{2} (\Delta_x E_2^{xz} + \Delta_x E_9^{xz}) + \frac{\hat{G}}{4} \Delta_x E_{xz}^n = -C_x Z_0 \frac{T}{2} (\Delta_y H_9^y - \Delta_y H_2^y)$$

where  $C_x$  can be found in Appendix B,  $\hat{G} = \hat{R}$  is given by (21), and  $T$  is a time-delay operator defined by  $TU^n = U^{(n-1)}$ . Samples are taken at time  $(n+1/2)\Delta t$  unless otherwise indicated. Thus, the operation  $TU$  denotes

the quantity  $U$  at time  $(n-1/2)\Delta t$ . Hence, (26) yields the value of  $E_{xz}^n$  as :

$$(27) \quad \Delta_x E_{xz}^n = \frac{4}{4+R} (a_{19} + a_{20})^{(n-1/2)}$$

in which :

$$(28) \quad \begin{cases} a_{19} \\ b_{19} \end{cases} = \frac{1}{2} (\Delta_x E_2^{xz} \mp C_x Z_0 \Delta_y H_2^n) \text{ and} \\ \begin{cases} a_{20} \\ b_{20} \end{cases} = \frac{1}{2} (\Delta_x E_9^{xz} \mp C_x Z_0 \Delta_y H_9^n)$$

The last step to evaluate the contribution of  $E_{xz}$  into  $E_x^n$  at the cell center, is to insert (27) into (B.1). This yields (30) which is the first algorithm expression described in the next section. Other relations are derived in a similar fashion.

To completely account for the influence of the sub-term  $E_{xz}$ , remains the evaluation of the evolution of  $b_{19}$  and  $b_{20}$  from incident voltages and field components at the center of the cell. To achieve this, one again integrates numerically (22) but, this time, from time  $(n-1/2)\Delta t$  and  $(n+1/2)\Delta t$  and spatially from  $(k-1/2)\Delta z$  and  $k\Delta z$  (from the face to the cell center). This yields :

$$(29) \quad \frac{(1-T)}{2} \Delta_x E_2^{xz} - \frac{(1+T)}{2} C_x Z_0 \Delta_y H_2^n \\ + \frac{\hat{G}}{4} \Delta_x E_{xz}^n = + C_x Z_0 \Delta_y H_y^n$$

In order to establish a new expression that contains  $b_{19}$  at time  $(n+1/2)\Delta t$  as a function of  $a_{19}$ ,  $a_{20}$  at time  $(n-1/2)\Delta t$  and the magnetic field component  $H_y$  ( $H_y^n$ ) at the cell center, (27) and (28) are introduced into (29). This yields (30) the first expression of the second group of the algorithm described in the next section. A spatial integration procedure between  $K\Delta z$  and  $(k+1/2)\Delta z$ , allows one to establish a relation similar to (29) from which  $b_{20}$  can be then computed. Finally, the same procedure is applied to all sub-terms yielding the generic PML-TLM cell which comprises  $18+8 = 26$  voltages as illustrated in Figure 2b.

At this point, it is important to stress that the TLM node developed above uses only set of conductivities (i.e.  $\sigma_z, \sigma_z^* \neq 0$ ). Some authors refer to uniaxial PML media. For simulating layers that completely surround the computational domain, it is customary to use all conductivities at corners, where three uniaxial PML (i.e., perpendicular to  $x, y, z$  axes, respectively) meet. A more general TLM node that accounts for all conductivities can be developed following exactly the above procedure. Such a node would include a total of 30 voltages. However, the problem of using multiaxial PML at corners is still under investigation and, consequently, not dealt with here.

#### IV.2.2 PML-TLM algorithm

As for the standard TLM node, the PML-TLM algorithm uses the accelerated procedure briefly described before.

According to (17), the only modification pertains to accounting for the source terms at the cell center and at time  $n\Delta t$ , by using typical expression such as (27) and new relations for reflected voltages  $\{b_{19}, \dots, b_{26}\}$ . Hence, relations (B.1) to (B.6) see Appendix B) become:

$$(30) \quad \Delta_x E_x^n = \left\{ C_x (a_1 + a_{12} + a_2 + a_9 + \hat{Y}_{sx} a_{13})^{(n-1/2)} \right. \\ \left. - \frac{\hat{G}}{4 + \hat{G}} (a_{19} + a_{20})^{(n-1/2)} \right\}$$

$$(31) \quad \Delta_y E_y^n = \left\{ C_y (a_3 + a_{11} + a_4 + a_8 + \hat{Y}_{sy} a_{14})^{(n-1/2)} \right. \\ \left. - \frac{\hat{G}}{4 + \hat{G}} (a_{21} + a_{22})^{(n-1/2)} \right\}$$

$$(32) \quad \Delta_z E_z^n = \left\{ C_z (a_5 + a_7 + a_6 + a_{10} + \hat{Y}_{sz} a_{15})^{(n-1/2)} \right.$$

$$(33) \quad Z_0 \Delta_x H_x^n = B \left\{ D_x (-a_4 + a_8 + a_5 - a_7 \right. \\ \left. + \hat{Z}_{sx} a_{16})^{(n-1/2)} + \frac{\hat{G}}{4} (a_{23} + a_{24})^{(n-1/2)} \right\}$$

$$(34) \quad Z_0 \Delta_y H_y^n = B \left\{ D_y (a_2 - a_9 - a_6 + a_{10} \right. \\ \left. + \hat{Z}_{sy} a_{17})^{(n-1/2)} + \frac{\hat{G}}{4} (a_{25} + a_{24})^{(n-1/2)} \right\}$$

$$(35) \quad Z_0 \Delta_z H_z^n = \left\{ D_z (-a_1 + a_{12} + a_3 - a_{11} \right. \\ \left. + \hat{Z}_{sz} a_{18})^{(n-1/2)} \right\}$$

where  $B$  and  $\hat{G} = \hat{R}$  are given by (21).

Then,  $\{b_{19}, \dots, b_{26}\}$  are computed using (B.10) in Appendix B and  $\{b_{19}, \dots, b_{26}\}$  from the expressions below:

$$(36) \quad b_{19}^{(n+1/2)} = -C_x Z_0 \Delta_y H_y^n + B a_{19}^{(n-1/2)} \\ - B \frac{\hat{G}}{4} a_{19}^{(n-1/2)}$$

$$(37) \quad b_{20}^{(n+1/2)} = +C_x Z_0 \Delta_y H_y^n + B a_{20}^{(n-1/2)} \\ - B \frac{\hat{G}}{4} a_{19}^{(n-1/2)}$$

$$(38) \quad b_{21}^{(n+1/2)} = +C_y Z_0 \Delta_x H_x^n + B a_{21}^{(n-1/2)} \\ - B \frac{\hat{G}}{4} a_{22}^{(n-1/2)}$$

$$(39) \quad b_{22}^{(n+1/2)} = -C_y Z_0 \Delta_x H_x^n + B a_{22}^{(n-1/2)} \\ - B \frac{\hat{G}}{4} a_{21}^{(n-1/2)}$$

$$(40) \quad b_{23}^{(n+1/2)} = -D_x \Delta_x E_z^n + a_{23}^{(n-1/2)}$$

$$(41) \quad b_{24}^{(n+1/2)} = +D_x \Delta_x E_z^n + a_{24}^{(n-1/2)}$$

$$(42) \quad b_{25}^{(n+1/2)} = +D_y \Delta_y E_z^n + a_{25}^{(n-1/2)}$$

$$(43) \quad b_{26}^{(n+1/2)} = -D_y \Delta_y E_z^n + a_{26}^{(n-1/2)}$$

Finally, to complete the procedure, the definition of voltages that model controlled sources is given in Appendix C.

#### IV.2.3 Boundary conditions

The algorithm for both TLM and TLM-PML nodes are now established. The last point pertains to determining incident voltages at nodes adjacent to the interface between the TLM and TLM-PML network. As far as the first eighteen voltages are concerned, they are treated by the basic TLM scheme [2]. For the remaining voltages, let us first consider the interface perpendicular to the  $z$ -axis (Fig. 4.a). In the TLM domain (region 1), there are two reflected voltages from the adjacent nodes, say  $b_2^{(1)}$  and  $b_4^{(1)}$ , that impinge on the interface at time  $(n + 1/2)\Delta t$ . On the other side in the PML medium (region 2), there are four voltages  $b_8^{(2)}$ ,  $b_{20}^{(2)}$ ,  $b_9^{(2)}$  and  $b_{22}^{(2)}$  reflected from the PML-TLM nodes adjacent of that interface (see Fig. 2). Concerning  $(b_2^{(1)}, b_9^{(2)})$  and  $(b_4^{(1)}, b_8^{(2)})$ , they are simply transferred across the interface for the next iteration [2]. On the other hand,  $b_{20}^{(2)}$  and  $b_{22}^{(2)}$  are not transferred through the interface as the TLM node in region 1 has only 18 voltages. However,  $a_{20}^{(2)}$  and  $a_{22}^{(2)}$  incident on TLM-PML node must be computed. First of all, note that the knowledge of  $(b_2^{(1)}, b_9^{(2)})$  and  $(b_4^{(1)}, b_8^{(2)})$  allows one to compute the field components tangential to the interface. Then, the magnetic field components  $H_x$  and  $H_y$  at time  $(n + 1/2)$  are given by (see (A. 1) in Appendix A):

$$(44) \quad Z_0 \Delta_x H_x^{(n+1/2)} = b_4^{(1)} - b_8^{(2)}$$

$$\text{and} \quad Z_0 \Delta_y H_y^{(n+1/2)} = b_9^{(2)} - b_2^{(1)},$$

Then,  $a_{20}^{(2)}$  and  $a_{22}^{(2)}$  can be computed from their definition (see (C. 1) in Appendix C):

$$(45) \quad \begin{aligned} a_{20}^{(2)} &= b_{20}^{(2)} - C_x Z_0 \Delta_y H_y^{(n+1/2)} \\ &= b_{20}^{(2)} - C_x (b_9^{(2)} - b_2^{(1)}) \end{aligned}$$

$$(46) \quad \begin{aligned} a_{22}^{(2)} &= b_{22}^{(2)} + C_x Z_0 \Delta_x H_x^{(n+1/2)} \\ &= b_{22}^{(2)} + C_x (b_4^{(1)} - b_8^{(2)}) \end{aligned}$$

Now, let us consider the case where the PML-TLM network is terminated by the vacuum intrinsic impedance  $Z_0$  in the plane perpendicular to  $x$ -axis. As the characteristic impedance of the TLM link lines is also  $Z_0$ , such termination means zero reflection in the link lines (note that the global reflection is not zero). At time  $(n + 1/2)\Delta t$   $b_3$ ,  $b_6$  and  $b_{25}$  impinge on the boundary (see Fig. 2b). Thus,  $a_3$  and  $a_6$  are zero and one can easily show that from the definition (A. 1) in Appendix A, the component  $E_z$  is given by:

$$(47) \quad \Delta_z E_z^{(n+1/2)} = b_6,$$

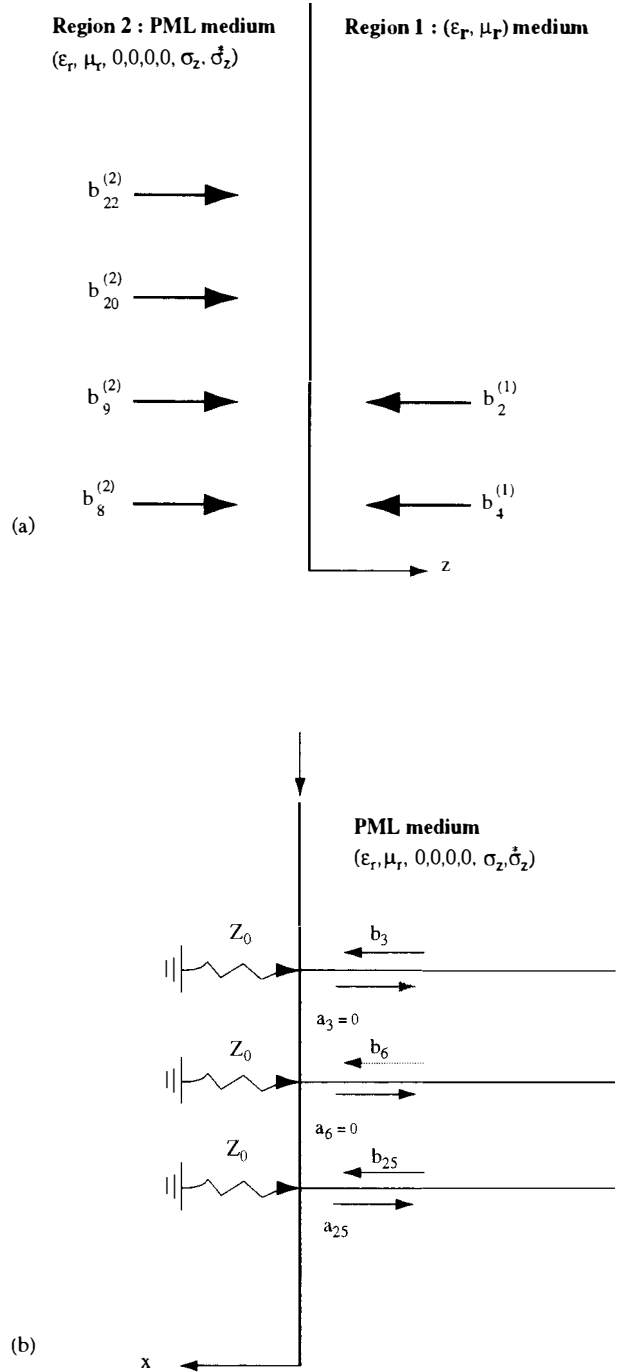


FIG. 4. — Voltage at PML boundaries (a) interface between TLM and PML-TLM networks (b) at the limit of the PML-TLM network terminated by  $Z_0$

*Tensions incidentes à la frontière du réseau PML-TLM : (a) interface entre le réseau TLM classique et le réseau PML-TLM (b) réseau PML-TLM termin par  $Z_0$*

Hence,  $a_{25}$  can be computed from:

$$(48) \quad a_{25} = b_{25} - D_y \Delta_z E_z^{(n+1/2)} = b_{25} - D_y b_6$$

The above procedures can be easily applied to other reflection coefficient values when a TLM-PML algorithm is used.

## V. RESULTS

### V.1. Matched layer results

#### V.1.1. Influence of the conductivity profile

The reflection coefficient is computed by using the SCN for different profiles (linear, geometric, ...) ARC and geometries (microstrip and coplanar). In addition, substrate with low and high permittivity is considered. The parabolic profile has been found to yield the best performances:

$$(49) \quad \sigma(z) = \sigma_{\max} \left( \frac{z}{\delta} \right)^2$$

However, as mentioned before, the discretization of the profile leads to an abrupt change in the conductivity value near the interface that provokes numerical reflections. An alternate profile, called semi-parabolic profile, has a factor five times lower than the parabolic profile, which reduces the conductivity step value near the interface and, consequently, the numerical reflections. However, since the penetrating wave must be sufficiently attenuated to obtain the same ARC, the conductivity profile has a much larger conductivity factor at the end of the layer. Simulation results shown below are performed with a  $15\text{-}\Delta l$  layer thickness, where  $\Delta l$  is the space step in the direction of propagation. This choice was found to be the best compromise between reflection and memory requirement.

Return loss extraction for microstrip and co-planar structures is performed using the geometries shown in Figure 5 with  $\Delta l = 100 \mu\text{m}$  and  $\Delta t = 0.1666 \text{ ps}$ . Side walls are  $15\Delta l$  from the central metal strip and are terminated by matched impedance. Note that a sufficiently

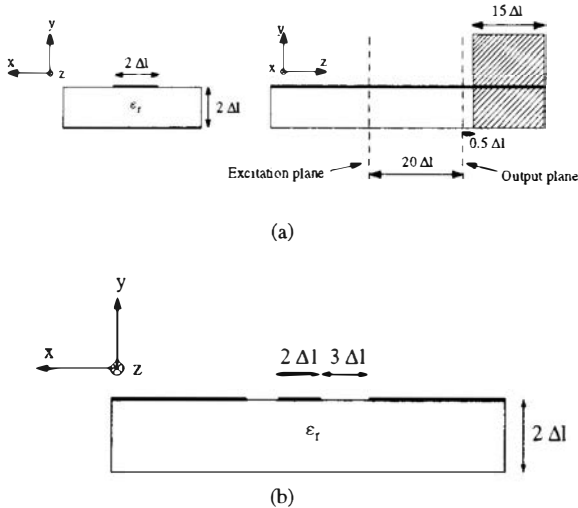


FIG. 5. — Geometry used for ML absorption performance : (a) microstrip line. (b) coplanar line.

Géométries utilisées pour le calcul du facteur de réflexion des ML. (a) microruban, (b) ligne coplanaire.

good spatial sampling must be used to describe the slot for co-planar line. If this condition is not fulfilled, the quasi-TEM mode is not accurately described, which results in a higher reflection level from the matched layer interface. It was found that three cells for describing the slots has produced sufficiently good results. Using a coarser mesh, return loss may get 20 dB lower in the examples presented below. Finally, excitation consisted of a Gaussian pulse whose variance was selected according to the desired frequency range characterization. Sources were located between the ground plane and the strip while they were across the slots in the coplanar lines (even mode).

First of all, simulations were performed on planar structures shown in Figure 5, with  $\epsilon_r = 2.2$ . For the microstrip case (Fig. 6a), the optimum layer corresponded to a 40 dB ARC (parabolic profile) and a computed reflection coefficient (CRC) which is always lower than  $-52 \text{ dB}$ . A slight decrease in absorption (still good), is obtained in the co-planar case illustrated in Figure 6b ( $-30 \text{ dB}$  ARC with  $-50 \text{ dB}$  CRC). For both cases, there is some substantial improvement as compared to standard matched boundaries. Finally, as mentioned before,

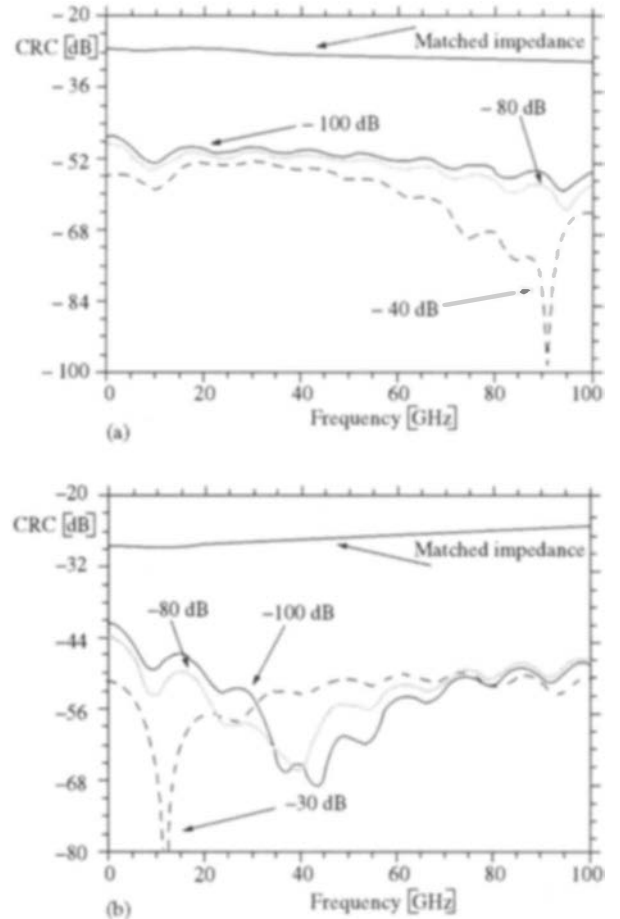


FIG. 6. — Matched layer crc (parabolic profile) for several arc values ( $\epsilon_r = 2.2$ ) : (a) microstrip line. (b) coplanar line.

Facteur de réflexion calculé du milieu ML à profil parabolique pour différents valeurs de ARC ( $\epsilon_r = 2.2$ ) : (a) microruban. (b) ligne coplanaire.

less reflection than the ARC value occurs because of the matched loads used at the back of the absorbing layer. Also, one can observe that the CRC increases as the ARC decreases. This can be explained by the fact that the adjacent conductivity ratio at the interface increases with ARC (see (11) with (49)).

Results have shown that the substrate permittivity did not influence the absorbing performance of the ML up to  $\epsilon_r = 6$ . However, as the permittivity increases further, the absorption performance slightly deteriorates. For instance, on the frequency range (0 – 100 GHz), results pertaining to two different substrates ( $\epsilon_r = 9.9$  and  $\epsilon_r = 12.8$ ) are reported in Figure 7. Optimal layer is obtained for a  $-30$  dB ARC, yielding a  $-46$  dB CRC. Results (not shown) are very similar for the co-planar line. Note that one can lower low-frequency reflection by decreasing the ARC down to  $-100$  dB (see Fig. 7). In this case, the CRC is lower than  $-50$  dB on the 0-30 GHz band. This result can be explained by the fact that quasi-TEM modes are closer to normal incidence in the low frequency range. On the other hand, semi-parabolic profile optimization may be performed on the high frequency range. Results compared with parabolic profile are given in Figure 8. A  $-50$  dB CRC is obtained on 30 to 100 GHz band, using a  $-100$  dB ARC.

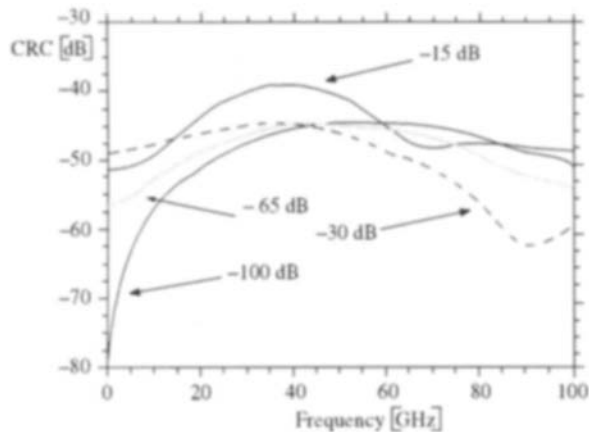


FIG. 7. — Matched layer crc (parabolic profile) for several arc values in the microstrip line case, with high permittivity substrate ( $\epsilon_r = 9.9$ ).

*Facteur de réflexion calculé du milieu ML (profil parabolique) pour différentes valeurs du facteur de réflexion apparent ARC dans le cas du microruban avec substrat à forte permittivité relative (9,9).*

From the above results, when dealing with high permittivity substrates, one can improve the absorption by using parabolic profile in the low frequency range and semi-parabolic profile in the high frequency range. However, results have shown that improvement with semi-parabolic profile is no longer efficient for co-planar guides. Finally, one should mention that the performance of ML for planar circuit's characterization is sufficient as a reflection level below  $-46$  dB is very good for S parameter extraction.

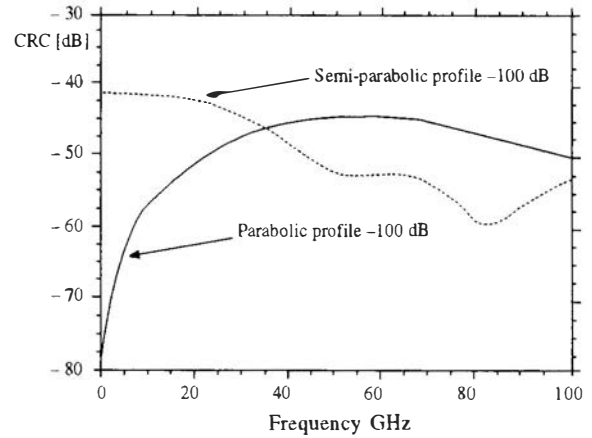


FIG. 8. — Matched layer crc (parabolic and semi-parabolic profile) for microstrip with high relative permittivity substrate (9.9).

*Facteur de réflexion calculé du milieu ML (profil parabolique et semi-parabolique) dans le cas du microruban avec substrat à forte permittivité relative (9.9).*

### V.1.2. Absorption performance for different TLM mode simulations

The various TLM SCN nodes have different dispersion characteristics and, in addition, some of them require additional interface condition between different media [18]. Figure 9 shows the comparison between the various SCN in the case of the microstrip line, with two different substrate permittivities ( $\epsilon_r = 2.2$  and  $9.9$ ). It can be observed that the overall performance of the SSCN is not as good as for other nodes, especially for high permittivity (Fig. 9a). These differences could be explained by the difference of the SSCN dispersion characteristic as compared to the HSCN and the SCN. This is confirmed by Figure 9b in which the performance shown by the HSCN and the SCN tends to be identical, likewise their dispersion characteristics for low permittivity values. Further investigations are necessary to find explanations on this issue.

### V.1.3. Planar circuits S-parameter computation

The S-parameters are computed with the basic SCN for the microstrip line loaded by an open stub shown in Figure 10. Results are compared with measurements in Figure 11. Excellent agreement is found in both magnitude and phase. Note that a 2% resonance frequency shift for  $S_{11}$  is observed. This phenomenon is well known in TLM modeling and is due to coarseness error as explained further. The resonant frequency shift was 2.1% and 2.4% for the HSCN and SSCN, respectively. They confirm the slightly lower accuracy produced by the SSCN. However, if one considers the very close performance obtained by the three nodes, one should mention the substantial memory gain of the HSCN and SSCN as compared to the SCN (17% and 33%, respectively). To conclude from the above results, the HSCN seems to be the best compromise in terms of memory and accuracy.

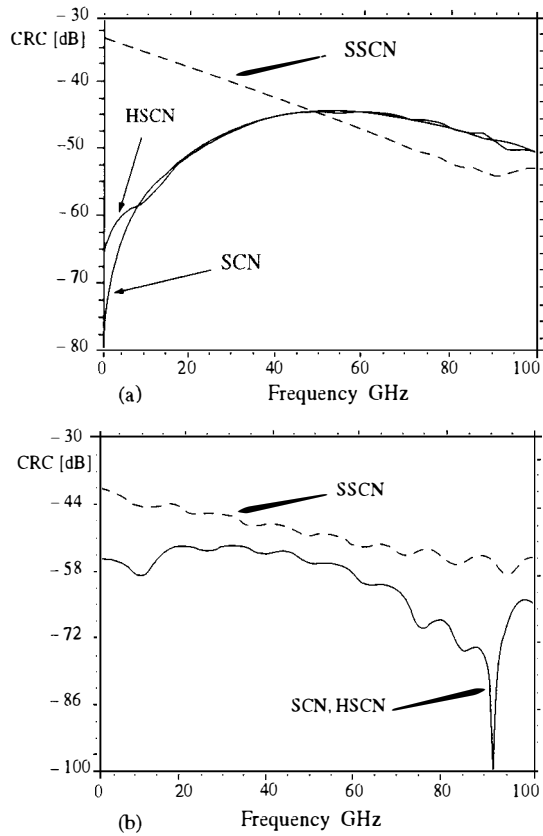


FIG. 9. — Matched layer reflection comparison of the three TLM nodes : (a) microstrip  $\epsilon_r = 9.9$ , ARC = -100 dB. (b) microstrip  $\epsilon_r = 2.2$ , ARC = -40 dB.

Comparaison des valeurs du facteur de réflexion calculé pour le milieu ML entre les trois cellules TLM : (a) microruban,  $\epsilon_r = 9.9$ , ARC = -100 dB. (b) microruban,  $\epsilon_r = 2.2$ , ARC = -40 dB.

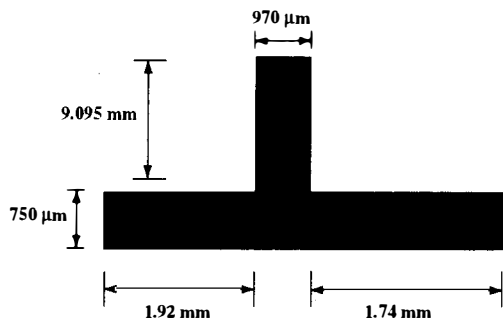


FIG. 10. — Microstrip discontinuity on a 254- $\mu\text{m}$  thick substrate with  $\epsilon_r = 2.2$ .

Discontinuité en microruban sur un substrat de hauteur 254  $\mu\text{m}$  et de permittivité relative 2,2.

## V.2. PML results

### V.2.1. Conductivity profile tests

The proposed model is tested for validation in the case of wide-band matched load simulation for  $\text{TE}_{10}$ -mode propagation in a empty rectangular waveguide (WR-28 with  $a = 32 \text{ mm} = 36 \Delta l$ ). This canonical case

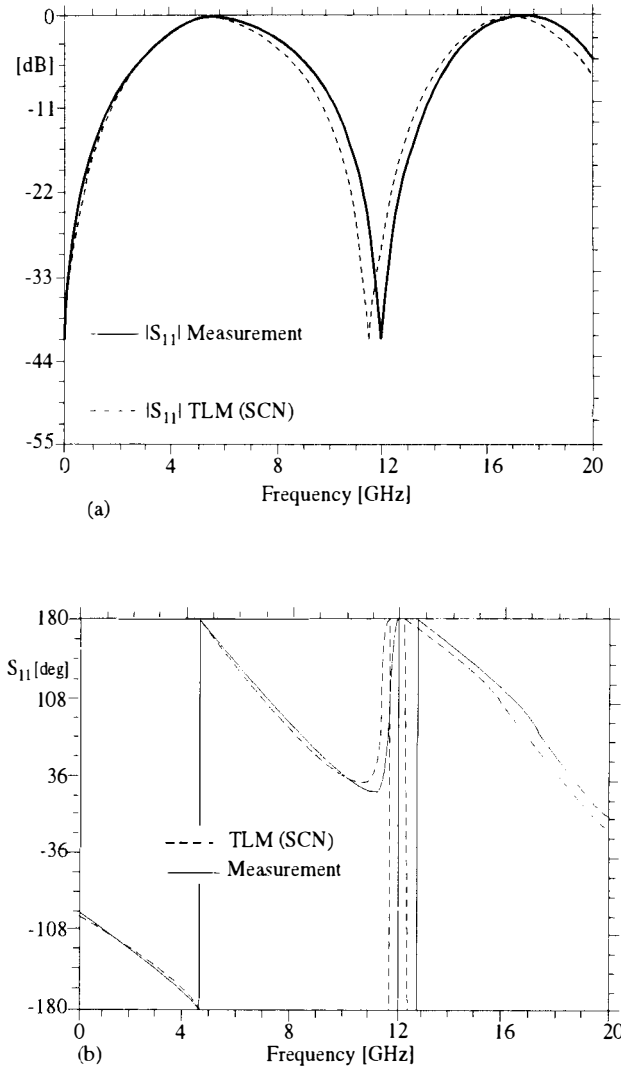


FIG. 11. —  $S_{11}$  scattering coefficient of the discontinuity illustrated in Figure 10, ( $\Delta l = 124 \mu\text{m}$ ,  $\Delta t = 1.97 \cdot 10^{-13} \text{ s}$ , 2500 iterations) with SCN-ML matched load simulation : (a) magnitude, (b) phase.

Paramètres de repartition  $S_{11}$  de la discontinuité de la figure 10 calculés avec des charges adaptées simulées par un milieu ML et la cellule SCN ( $\Delta l = 124 \mu\text{m}$ ,  $\Delta t = 1.97 \cdot 10^{-13} \text{ s}$ , 2500 itérations) : (a) module. (b) phase.

is very relevant to testing absorbing conditions. Indeed, all cases of incidence can be achieved (except near to normal), including evanescent modes. The guide is excited by a current sheet [14] which is located near the PML interface (Fig. 12). The conductivity profile used in the PML is parabolic with  $\sigma_{\text{max}} = 25 \text{ S/m}$ . The time excitation is a Gaussian pulse to achieve wideband characterization centered on the dominant mode operating range. Output points from which time sequences are extracted are  $P_1$  and  $P_2$  (fig. 12). A FFT procedure is applied to obtain the frequency characteristics. Results shown in Figure 12 yield a reflection coefficient which is lower than -58 dB over the 25-40 GHz frequency range. This shows some significant improvement as compared to reflection levels reported with other ABC used in TLM [3].

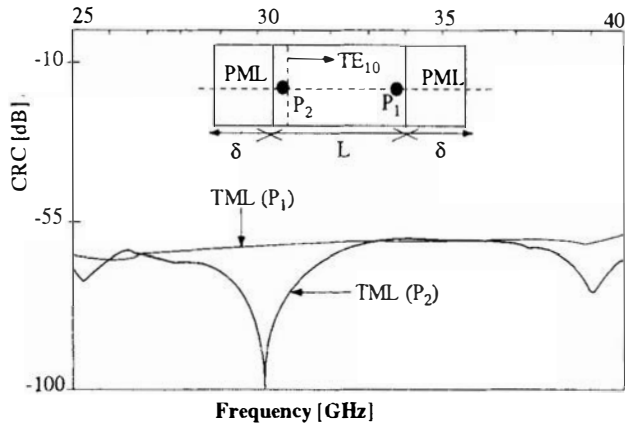


FIG. 12. — Reflection coefficient from the PML medium used as matched loads in a WR-28 rectangular waveguide ( $\sigma_{\max} = 25 \text{ S/m}$ ,  $L = 60 \Delta l$ ,  $\delta = 20 \Delta l$ ,  $a = 36 \Delta l$ ,  $P_1$  and  $P_2$  located at one  $\Delta l$  from the PML interface).

Facteur de réflexion pour la propagation du mode dominant dans un guide d'ondes terminé par des PML ( $\sigma_{\max} = 25 \text{ S/m}$ ,  $L = 60 \Delta l$ ,  $\delta = 20 \Delta l$ ,  $a = 36 \Delta l$ ,  $P_1$  et  $P_2$  placés à un  $\Delta l$  de l'interface).

### V.2.2. S-parameters extraction

The next canonical case is the wide-band characterization of a capacitive iris in a WR-28 rectangular waveguide in which PML technique described above is used for matching. The magnitude of  $S_{11}$  is shown in Figure 13 in which FDTD [10] and the proposed unified TLM technique are compared with a closed-form solution used as reference [21]. Some slight discrepancies can be observed with the reference for both numerical methods, in particular the TLM. This is due to the presence of sharp edges near the iris where field gradients are high and for

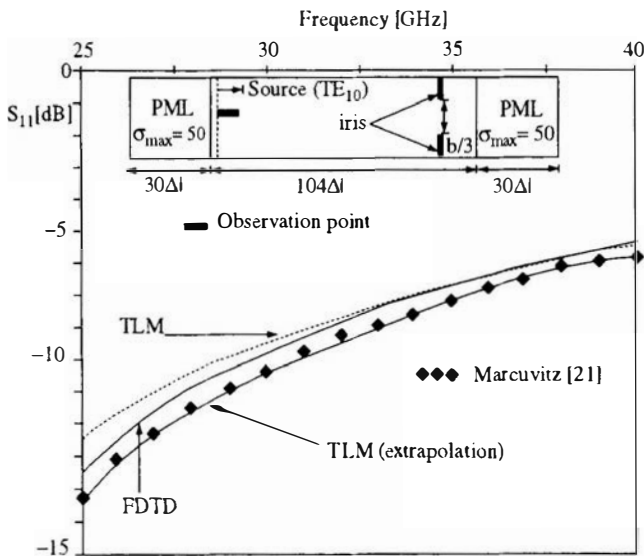


FIG. 13. — Computed reflection coefficient (CRC) for a capacitive iris in a WR-28 rectangular waveguide terminated by PML ( $a = 66 \Delta l$  for the fine mesh).

Facteur de réflexion calculé pour un iris capacitif dans un guide d'ondes wr-28 terminé par des pml ( $a = 66 \Delta l$  pour le maillage fin).

which the TLM produces some additional error as compared to FDTD [22]. In order to reduce this error, an extrapolation technique is applied. From two successive simulations using finer mesh size, results for the zero mesh-size limit are extrapolated. This technique yields excellent results as shown in Figure 13. It is important to notice that PML interface is located close to the iris where evanescent higher-order modes prevail. It seems to indicate that PML can absorb evanescent modes. Finally, some cases of instabilities for iris simulations were observed when fine mesh was used. This problem could be resolved by decreasing the time-step. This resulted in an increase of the number of iterations and, thus, of the computation time. The source of instabilities is currently under investigation.

The next case for validation pertains to planar circuits shown in Figures 14 and 15. In both cases, the PML are used as matched loads in the direction of propagation. In other sides, both PLM and PML-TLM networks are terminated by  $Z_0$ . Results for S-parameters are presented in Figure 14, where they are compared with those obtained with the FDTD-PML unified algorithm and measurements [23]. Some good agreement can be observed up to 15 GHz. Beyond that frequency, the comparison should be considered with caution as the authors mentioned that the measurements were not reliable.

Finally, the example of the patch antenna (Fig. 15) is used to test the ability of the PML technique when the layer is located in the very near field (evanescent waves). For this purpose, the PML interface is located within two cells from the antenna edges perpendicular to the microstrip line. Results pertaining to the input reflection coefficient are shown in (Fig. 15). Comparison with PML interface located 10 cells from the antenna showed only a slight difference of 0.3 dB at the first resonance. One may conclude that PML can be located very near the structure without affecting the accuracy

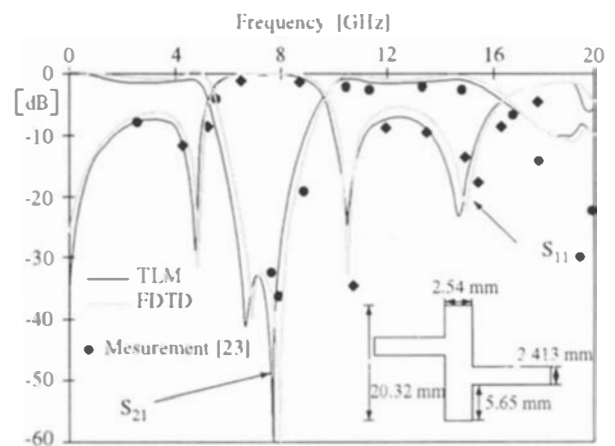


FIG. 14. — S-parameters of a microstrip filter (substrate :  $h = 0.794 \text{ mm}$ ,  $\epsilon_r = 2.2$ ) computed with PML matched load simulation.

Paramètres S d'un filtre microruban (substrat :  $h = 0.794 \text{ mm}$ ,  $\epsilon_r = 2.2$ ) terminé par des PML.

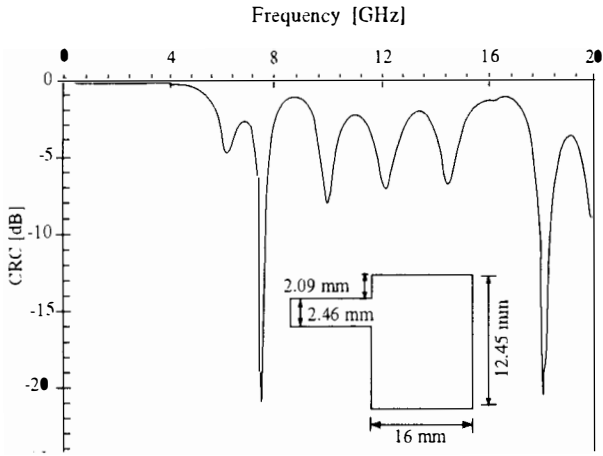


FIG. 15. — Input reflection coefficient of a patch antenna fed by a microstrip line (substrate :  $h = 0.794$  mm,  $\epsilon_r = 2,2$ ) computed with PML used as absorbing boundary conditions (ABC).

*Facteur de réflexion à l'entrée d'une antenne plaque alimentée par un microruban (substrat :  $h = 0,794$  mm,  $\epsilon_r = 2,2$ ) et avec des PML comme conditions aux limites absorbantes.*

that pertains to input impedance computation. Consequently, the computational domain can be reduced which produces some significant reduction of the computational cost, as compared to other ABC techniques.

## VI. CONCLUSION

Simulation of absorbing media with a unified TLM algorithm was presented. The matched layer technique was found to be very attractive in applications that involve wide-band matched loads of guides that operate in quasi-TEM situation. In this case, the absorbing medium can be simulated directly with the basic TLM algorithms (SCN, HSCN and SSCN) without modification. When quasi-normal incidence assumption is no longer valid, the perfectly matched layer technique (PML) must be rather used. A new TLM cell capable of simulating uniaxial PML media was introduced. It is an extension of the classical TLM-SCN and, thus ensures the continuity of the algorithm across the TLM-PML network interface. The concept of sources controlled by local fields was used and translated in terms of additional voltages (stubs) connected to the basic SCN. An accelerating procedure was applied for reducing the number of operations per iteration and boundary treatment for the new PML-TLM cell presented.

Simulation results in the case of planar circuits such as microstrip and co-planar lines, showed that ML technique yields 45 dB return loss, at least, over the frequency range up to 100 GHz and relative permittivity substrate up to 6. For a higher value of  $\epsilon_r$ , return loss decreases but is still at a good level for practical purposes. All TLM node simulations of ML showed numerical stability. Finally, the TLM SSCN node is less performant than other cells but requires less memory than the other nodes.

The new TLM-PML cell was found to be efficient for simulation of general matched load. In addition, it was found that the PML was able to be located where evanescent waves prevailed which was not the case for other absorbing techniques currently used in TLM. In certain solutions, numerical instabilities occurred but could be circumvented by reducing the time step at the price of increasing the number of iterations. The source of this problem is currently under investigation.

*Manuscrit reçu le 15 octobre 1997*

## Appendix A: Incidence and reflected voltage definition for the TLM-SCN

Incident voltage vector ( $\vec{a}$ ) and reflected voltage vector ( $\vec{b}$ ) are defined from field samples shown in Figure 1 [14] :

$$(A.3) \quad \left\{ \begin{array}{c} \vec{a} \\ \vec{b} \end{array} \right\} = \frac{1}{2} \left[ \begin{array}{c} \Delta_x E_1^x \mp Z_0 \Delta_z H_1^z \\ \Delta_x E_2^x \pm Z_0 \Delta_y H_2^y \\ \Delta_y E_3^y \pm Z_0 \Delta_z H_3^z \\ \Delta_y E_4^y \mp Z_0 \Delta_x H_4^x \\ \Delta_z E_5^z \pm Z_0 \Delta_x H_5^x \\ \Delta_z E_6^z \mp Z_0 \Delta_y H_6^y \\ \Delta_z E_7^z \mp Z_0 \Delta_x H_7^x \\ \Delta_y E_8^y \pm Z_0 \Delta_x H_8^x \\ \Delta_x E_9^x \mp Z_0 \Delta_y H_9^y \\ \Delta_z E_{10}^z \pm Z_0 \Delta_y H_{10}^y \\ \Delta_y E_{11}^y \mp Z_0 \Delta_z H_{11}^z \\ \Delta_x E_{12}^x \pm Z_0 \Delta_z H_{12}^z \\ \vec{V}_E \\ \vec{V}_M \end{array} \right]$$

$$\text{where } \vec{V}_E = \left[ \begin{array}{c} \Delta_x E_{13}^x \\ \Delta_y E_{14}^y \\ \Delta_z E_{15}^z \end{array} \right] \quad \text{and } \vec{V}_M = \left[ \begin{array}{c} Z_0 \Delta_x H_{16}^x \\ Z_0 \Delta_y H_{17}^y \\ Z_0 \Delta_z H_{18}^z \end{array} \right]$$

## Appendix B: Accelerated procedure for ( $\vec{b}$ ) calculation [14]

First of all, the field components at the cell center are computed at time  $n\Delta t$  from ( $\vec{a}$ ) known at time  $(n-1)\Delta t$  and adding the source contribution at time  $n\Delta t$ :

$$(B.1) \quad \Delta_x E_x^n = A_x \left\{ C_x (a_1 + a_{12} + a_2 + a_9 + \hat{Y}_{sx} a_{13})^{(n-1/2)} - \frac{1}{4} \frac{Z_0^s}{4\epsilon_{xx}} \Delta_x J_{ex}^n \right\}$$

$$(B.2) \quad \Delta_y E_y^n = A_y \left\{ C_y (a_3 + a_{11} + a_4 + a_8 + \hat{Y}_{sy} a_{14})^{(n-1/2)} - \frac{1}{4} \frac{Z_0^s}{4\epsilon_{yy}} \Delta_y J_{ey}^n \right\}$$

$$(B.3) \quad \Delta_z E_z^n = A_z \left\{ C_z (a_5 + a_7 + a_6 + a_{10} + \hat{Y}_{sz} a_{15})^{(n-1/2)} - \frac{1}{4} \frac{Z_0^s}{4\epsilon_{zz}} \Delta_z J_{ez}^n \right\}$$

$$(B.4) \quad Z_0 \Delta_x H_x^n = B_x \left\{ D_x (-a_4 + a_8 + a_5 - a_7 + \hat{Z}_{sx} a_{16})^{(n-1/2)} - \frac{1}{4} \frac{s}{\mu_{xx}} \Delta_x J_{mx}^n \right\}$$

$$(B.5) \quad Z_0 \Delta_y H_y^n = B_y \left\{ D_y (a_2 - a_9 - a_6 + a_{10} + \hat{Z}_{sy} a_{17})^{(n-1/2)} - \frac{1}{4} \frac{s}{\mu_{yy}} \Delta_y J_{my}^n \right\}$$

$$(B.6) \quad Z_0 \Delta_z H_z^n = B_z \left\{ D_z (-a_1 + a_{12} + a_3 - a_{11} + \hat{Z}_{sz} a_{18})^{(n-1/2)} - \frac{1}{4} \frac{s}{\mu_{zz}} \Delta_z J_{mz}^n \right\}$$

where  $\Delta t$  is the time step,  $s = 2c_0 \Delta t$  with  $c_0$  the free space velocity of light. Factors  $C_\xi$  and  $D_\xi$  are given by:

$$C_\xi = \frac{s \Delta_\xi}{2\epsilon_{\xi\xi} \Delta_\eta \Delta_\zeta} \quad \text{and} \quad D_\xi = \frac{s \Delta_\xi}{2\mu_{\xi\xi} \Delta_\eta \Delta_\zeta}$$

where  $(\xi, \eta, \zeta) \in \{(x, y, z), (y, z, x), (z, x, y)\}$ . Stub normalised admittances  $(\hat{Y}_{s\xi} \text{ and } \hat{Z}_{s\xi})$  are given by :

$$(B.7) \quad \hat{Y}_{s\xi} = 4 \left( \frac{2}{C_\xi} - 1 \right) \quad \text{and} \quad \hat{Z}_{s\xi} = 4 \left( \frac{2}{D_\xi} - 1 \right)$$

with  $\xi \{x, y, z\}$

$$(B.8) \quad A_\xi = \frac{4}{4 + \hat{G}_\xi}$$

where the normalized conductance  $\hat{G}_\xi = \frac{Z_0^s \sigma_{e\xi}}{\epsilon_{\xi\xi}}$  and

$$(B.9) \quad B_\xi = \frac{4}{4 + \hat{R}_\xi}$$

where the normalized resistance  $\hat{R}_\xi = \frac{1}{Z_0^s} s \frac{\sigma_{m\xi}}{\mu_{\xi\xi}}$ .

Finally, sources  $(J_{e\xi}^n, J_{m\xi}^n)$  correspond to a spatial average value [14] at time  $n \Delta t$  which can be interpreted as value at the cell center.

The next step consists of combining the field values

computed above in the reflected voltage vector  $\vec{b}_c^n$  whose expression is given by (A.1) in Appendix A. Finally, one can show [14] that reflected voltages at time  $(n + 1/2) \Delta t$  can be computed as follows :

$$(B.10) \quad \vec{b}^{(n+1/2)} = \vec{b}_c^n - \vec{a}_p$$

where

$$\vec{a}_p = \{a_{12}, a_9, a_{11}, a_8, a_7, a_{10}, a_5, a_4, a_2, a_6, a_3, a_1, a_{13}, a_{14}, a_{15}, a_{16}, a_{17}, a_{18}\}^T$$

Finally, one should notice that the time step  $\Delta t$  is selected as the maximum value for which normalized immittances are real positive in every cell. This can be interpreted as the numerical stability criterion for the TLM method.

### Appendix C: Definition of additional voltages for the PML medium

Incident ( $\vec{a}_{\text{PML}}$ ) and reflected ( $\vec{b}_{\text{PML}}$ ) voltage vectors added to the SCN for the modeling of PML media are given below :

$$(C.1) \quad \vec{a}_{\text{PML}} = \frac{1}{2} \begin{bmatrix} a_{19} \\ a_{20} \\ a_{21} \\ a_{22} \\ a_{23} \\ a_{24} \\ a_{25} \\ a_{26} \end{bmatrix} = \frac{1}{2} \begin{bmatrix} \Delta_x E_2^{xz} + C_x Z_0 \Delta_y H_2^y \\ \Delta_x E_9^{xz} - C_x Z_0 \Delta_y H_9^y \\ \Delta_y E_4^{yz} - C_y Z_0 \Delta_x H_4^x \\ \Delta_y E_8^{yz} + C_y Z_0 \Delta_x H_8^x \\ Z_0 \Delta_x H_5^{xy} + D_x \Delta_z E_5^z \\ Z_0 \Delta_x H_7^{xy} - D_x \Delta_z E_7^z \\ Z_0 \Delta_y H_6^{yx} - D_y \Delta_z E_6^z \\ Z_0 \Delta_y H_{10}^{yx} + D_y \Delta_z E_{10}^z \end{bmatrix}$$

$$\vec{b}_{\text{PML}} = \frac{1}{2} \begin{bmatrix} b_{19} \\ b_{20} \\ b_{21} \\ b_{22} \\ b_{23} \\ b_{24} \\ b_{25} \\ b_{26} \end{bmatrix} = \frac{1}{2} \begin{bmatrix} \Delta_x E_2^{xz} - C_x Z_0 \Delta_y H_2^y \\ \Delta_x E_9^{xz} + C_x Z_0 \Delta_y H_9^y \\ \Delta_y E_4^{yz} + C_y Z_0 \Delta_x H_4^x \\ \Delta_y E_8^{yz} - C_y Z_0 \Delta_x H_8^x \\ Z_0 \Delta_x H_5^{xy} - D_x \Delta_z E_5^z \\ Z_0 \Delta_x H_7^{xy} + D_x \Delta_z E_7^z \\ Z_0 \Delta_y H_6^{yx} + D_y \Delta_z E_6^z \\ Z_0 \Delta_y H_{10}^{yx} - D_y \Delta_z E_{10}^z \end{bmatrix}$$

## REFERENCE

- [1] JOHNS (P. B.). A symmetrical condensed node for the TLM method. *IEEE Trans. Microwave Theory Tech.*, **35**, n° 4, pp. 370-377 (1987).
- [2] HOEFER (W. J. R.). The transmission line matrix method theory and applications. *IEEE Trans. Microwave Theory Tech.*, **33**, n° 10, pp. 882-893 (1985).
- [3] ESWARAPPA (Ch.), HOEFER (W. J. R.). Absorbing boundary conditions for time-domain TLM and FDTD analysis of electromagnetic structures. *Electromagnetics*, **16**, n° 5, pp. 489-519 (1996).
- [4] MORENTE (J. A.), PORTI (J. A.), KHALLADI (M.). Absorbing boundary conditions for the TLM method. *IEEE Trans. Microwave Theory Tech.*, **40**, n° 11, pp. 2095-2099 (1992).
- [5] CHEN (Z.), NEY (M. M.), HOEFER (W. J. R.). Absorbing and connecting boundary conditions for the TLM method. *IEEE Trans. Microwave Theory Tech.*, **41**, n° 11, pp. 2016-2024 (1993).
- [6] LE MAGUER (S.), PEÑA (N.), NEY (M.). Étude des couches adaptées pour le calcul des paramètres S de structures planaires en TLM 3D. *NUMELEC 97*, Lyon, (Mar. 1997).
- [7] BERENGER (J. P.). A perfectly matched layer for the absorption of electromagnetic waves. *J. Comput. Phys.*, **114**, n° 2, pp. 110-117 (1994).
- [8] BERENGER (J. P.). A perfectly matched layer for free-space simulation in finite-difference computer codes. *Ann. Télécommunic.*, **51**, n° 1-2, pp. 39-46 (1996).
- [9] ESWARAPPA (Ch.), HOEFER (W. J. R.). Implementation of Bérenger absorbing boundary conditions in TLM by interfacing FDTD perfectly matched layers. *Electronic Letters*, **31**, n° 15, pp. 1264-1266 (1995).
- [10] PEÑA (N.), NEY (M.). Absorbing boundary conditions using perfectly matched layer (PML) technique for three-dimensional TLM simulations. *IEEE Trans. Microwave Theory Tech.*, **45**, n° 10 (1997).
- [11] PEÑA (N.), NEY (M.). A new TLM Node for Bérenger's perfectly matched layer. *IEEE Microwave and Guided Wave Letters*, **6**, n° 11, pp. 410-412 (1996).
- [12] VEIHL (J. C.), MITTRA (R.). An efficient implementation of Bérenger's perfectly matched layer (PML) for finite-difference time-domain mesh truncation. *IEEE Microwave and Guided Wave Letters.*, **6**, n° 11, pp. 94-96 (1996).
- [13] ZHAO (L.), CANGELLARIS (A. C.). A general approach for the development of unsplit-field time-domain implementations of perfectly matched layer for FDTD grid truncation. *IEEE Microwave and Guided Wave Letters*, **6**, n° 5, pp. 209-211 (1996).
- [14] PEÑA (N.), NEY (M.). A general formulation of a three-dimensional TLM condensed node with the modeling of electric and magnetic losses and current sources. *12th Annual Review of Progress in Applied Computational Electromagnetics*, Monterey, pp. 262-269 (1996).
- [15] TRENKIC (V.). Efficient Computation Algorithms for TLM. *First Int. Workshop on TLM Modeling*, pp. 77-80 (1995).
- [16] SCARAMUZZA (R.), LOWERY (A. J.). Hybrid symmetrical condensed node for the TLM method. *Electronics Letters*, **26**, n° 23, pp. 1947-1948 (1990).
- [17] TRENKIC (V.), CHRISTOPOULOS (C.), BENSON (T. M.). Theory of the symmetrical super-condensed node for the TLM method. *IEEE Trans. Microwave Theory Tech.*, **43**, n° 6, pp. 1342-1348 (1995).
- [18] NEY (M. M.). Modeling of highly conducting boundaries with TLM. *electromagnetics*, **16**, n° 5, pp. 521-535 (1996).
- [19] BERENGER (J. P.). Calcul de la diffraction à l'aide d'une méthode aux différences finies. *Actes du colloque CEM*, Trégastel, France (1983).
- [20] BAHR (A.), LAUER (A.), WOLFF (I.). Application of the PML absorbing condition to the FDTD analysis of microwave circuits. *IEEE MTT-S Digest, TU-1B*, pp. 27-30 (1995).
- [21] MARCUVITZ (N.). Waveguide handbook, MA: Boston Technical Publishers (1964).
- [22] HERRING (J. L.), HOEFER (W. J. R.). Accurate modelling of zero thickness septa with the symmetrical condensed node. *First Int. Workshop on TLM Modeling*, pp. 237-240 (1995).
- [23] SHEEN (D.), ALI (S. M.), ABOUZAHERA (M.), KONG (J.). Application of the three-dimensional finite-difference time-domain method to the analysis of planar microstrip circuits. *IEEE Trans. Microwave Theory Tech.*, **38**, n° 7, pp. 849-857 (1990).